



**national accelerator laboratory**

NAL-Pub-73/89-EXP-THY  
2500.000

(Submitted to Nucl. Instr. and Methods)

**HIGH RESOLUTION CRYOGENIC SPARK CHAMBERS**

M. Atac and W. E. Taylor  
National Accelerator Laboratory  
Batavia, Illinois 60510

November 1973



## HIGH RESOLUTION CRYOGENIC SPARK CHAMBERS

M. Atac and W. E. Taylor  
National Accelerator Laboratory, Batavia, Illinois 60510

### SUMMARY

A cluster of four narrow gap (2.5 mm) spark chambers containing 8 wires per millimeter has been built and operated at low temperatures (as low as 118°K). Results obtained from these chambers indicate that the width of the spark column is reduced at lower temperatures due to the increased gas density. Electron diffusion and deviation of the spark column from the true particle trajectory are greatly reduced at lower temperatures with narrow gap spark chambers. Space resolutions less than  $\sigma = 70$  microns (HWHM) have been achieved and even better resolutions are predicted from the observed temperature dependence.

### INTRODUCTION

In the last few years increased attention has been directed to improve space resolution of detectors due to the fact that higher energy accelerators are being built and operated. The National Accelerator Laboratory in Batavia, Illinois has produced proton beams at 400 GeV energies. At such energies secondary particles are produced in a very narrow forward cone. Thus, tagging beam particles in space with high space resolution and detecting the direction of the secondary particle tracks with high accuracies become important.

Our preliminary results obtained from a single spark chamber indicate that space resolution in detecting particle tracks is improved substantially at low temperatures.<sup>1</sup> We were encouraged by the results and built a cluster of four spark chambers enclosed in a simple polyurethane liquid nitrogen cryostat.

Two fundamental effects may contribute to higher accuracies in determining particle tracks in spark chambers operating at low temperatures:

- a) Increased spark chamber gas density,
- b) Reduced thermal energy of gas atoms.

The first effect allows us to reduce the spark chamber gap since at low temperatures more primary electrons are produced per unit path length during the passage of a charged particle. A smaller gap results in decreased spread of a spark column. The mean free paths for the collisions between the electrons and the gas atoms become smaller at lower temperatures which reduces the diffusion of electrons during the spark formation. The second effect reduces the diffusion of electrons before a high voltage is applied to the chamber. This effect and operating at atmospheric pressure are the main advantages over highly pressurized spark chambers in which the resolution may be limited by multiple scattering depending on the window thickness of the pressure container.<sup>2</sup>

#### CONSTRUCTION

Figure 1 is a simplified cross-sectional view of the cryostat-spark chamber assembly showing the four one

dimensional spark chambers and the polyurethane enclosure. Liquid nitrogen vapor is used for cooling the spark chambers. Each chamber in the cryostat can be translated and rotated for visual alignment. A more detailed view of the spark chamber illustrated in Figure 2 shows a 10 micron thick photo etched copper wire-plane printed on a 125 micron kapton film. The 3 x 5 cm<sup>2</sup> sensitive area of the spark chamber plane contains 8 wires per millimeter, which is expanded by a factor of 4 in the magnetostrictive pickup region. The fiducial lines are positioned on both sides of the cryostat.

The temperature in the cryostat is set and maintained by a servo system with a chromel-constantan temperature sensor. When the temperature rises above a set value a solenoid valve is activated to transfer liquid nitrogen to the copper pan until the temperature returns to this value. This is repeated to insure a stable temperature within the cryostat.

90% Ne + 10% He gas is precooled through copper tubes in the cryostat and then slowly flows through the spark chambers at a rate of 10 cc per minute.

#### OPERATION

The spark current sensed by a magnetostrictive delay line 0.25 mm distance from the wire plane produced sonic pulses which were detected through a 0.5 mm wide pickup coil (8 turns). These pulses were then amplified and processed by a commercial 40 MHz scaler readout system used

to determine the center of gravity of the spark pulse along the wire plane.<sup>3</sup>

A high voltage thyatron pulser provided the high voltage pulses to the spark chambers with about a 30 nsec rise time. Sixty feet of RG8/U coaxial cables were used as transmission line storage capacitors. The spark chambers were tested at the Alternating Gradient Synchrotron of the Brookhaven National Laboratory using an unseparated  $\pi^-$  (7 GeV/c) beam contaminated with low energy particles from a lead absorber upstream from the detector. The beam passing through the active area of the spark chambers was defined by two 2 x 2 cm<sup>2</sup> plastic scintillators. The coincidence pulses obtained from these scintillators triggered the thyatron. Figure 3 shows the spark voltage threshold at various temperatures as the Ne-He mixture was flowing through the spark chambers. It has been observed that the speed of the sonic pulses along the magnetostrictive lines increases by 0.0027% per degree centigrade. This was correlated to a decrease in the scaler count as the cryostat temperature was lowered.

#### RESULTS

Particle trajectories sensed by the magnetostrictive readouts of three parallel wire planes were analyzed by subtracting the average of the first and third coordinates from the second to yield a deviation from a linear track through the wire chambers. From a scattergram of the deviations as a function of the slope of the track,

$(x_3 - x_1)$ , the centroid of the resulting distribution determined the relative translational displacements of the wire planes provided a majority of the slopes were in a preferred direction. The scattergram plot shown in Figure 4 was positioned about the centroid to produce a distribution of deviation from which the  $\sigma$  was measured as half width at half maximum. The distribution will be broadened by relative rotations of the planes about the beam axis; however this effect is expected to be small (less than 33 microns) and, thus, was not considered in the data reduction. Another effect which was, however, taken into account was deviations from particle trajectories with a deflection at the center wire plane producing angles as large as five degrees. Since the planes were evenly spaced it was determined that the resulting deviations would be related to the calculated "slope" of the track by a factor of  $\pm 1/2$  as observed in Figure 4. These data, although not taken as linear trajectories were included in the distribution. The procedure was repeated for decreasing chamber temperatures to obtain a relationship between resolution and temperature.

The spatial resolution of a single wire plane may be determined since the linear deviation is

$$\Delta x = x_2 - (x_1 + x_3)/2 \quad (1)$$

where  $x_1$ ,  $x_2$ , and  $x_3$  are the coordinates in the three wire planes respectively. Thus

$$\sigma_x^2 = \sigma_{x_2}^2 + (1/2)^2 \sigma_{x_1}^2 + (1/2)^2 \sigma_{x_3}^2 \quad (2)$$

hence for identical planes the spatial resolution of a single chamber is .8165 of that obtained by fitting linear tracks with the three chambers.

The frequency of the deviations of particle tracks from a straight line is shown in Figure 5 for various temperatures with a minimum  $\sigma = 70$  microns at 118°K.

The efficiency which remained about 100% over a 1 kV wide plateau above the spark voltage threshold was measured as a function of delay time at the various temperatures with no applied clearing field. The high voltage pulses applied to the chambers were delayed up to 3 microseconds beyond the transit time of the particle. The efficiency of the spark chamber approaches 100% at 173°K as shown in Figure 6 with a delay of 230 nsec while it drops to 50% for a delay of 1330 nsec and about 5% at 2 microseconds. Only a slight overall variation of the efficiency as a function of temperature was indicated over the range studied.

#### THEORY

The spatial resolution of the wire chambers is primarily affected by the thermal diffusion of electrons which are created by the passage of a beam particle through the chamber. This diffusion process was treated with standard techniques<sup>4</sup> for electrons in thermal equilibrium with the gas mixture. Using the number of ion pairs formed by a particle passing through the gas from an experiment by K. Skolil<sup>5</sup> with cosmic ray muons and the ionization energy loss of the particle predicted by the Bethe-Bloch formula<sup>6</sup>

the electron's average energy can be estimated to determine the time necessary for thermalization. Typical times for thermalization to be approached were calculated using an expression given by M. Biondi<sup>7</sup> for rate of electron energy loss in neon and are seen to be within the minimum delay time of the readout system as shown in Figure 7.

The diffusion velocity for thermalized electrons is determined using the method of analysis by M. Biondi<sup>8</sup> giving

$$-D\left(\frac{\partial n}{\partial x}\right)_t = nv_x \quad (3)$$

Here D is the electron diffusion coefficient as measured by J. Lloyd<sup>9</sup> and is plotted in Figure 8. The time dependence of the electron density satisfies the equation

$$n = \frac{n_o}{(1 + \alpha n_o t)} \quad (4)$$

This equation has been shown to be valid where the dominant process is electron recombination with gas atoms particularly for high initial electron densities<sup>10</sup>,  $n_o$ .

Although the spatial form of the charge density is not known analytically since it depends on the initial electron distribution as well as the geometry of the chamber, the electrons are assumed to experience elastic scattering during the process of diffusion which may relate particle flux to the charge density in the form  $e^{-pP_c x}$ . Where  $P_c$  is the elastic collision probability measured by A. Salop<sup>11</sup> and earlier by C. Normand<sup>12</sup> for low-energy electron scattering in neon, and p is the gas pressure.

The electron absorption coefficient  $\alpha$  is given by M. Langevin<sup>13</sup> for high density gases as



$$\alpha = \frac{e}{\epsilon_0} \mu \quad (5)$$

where  $\mu$  is the electron mobility from the Einstein relation<sup>14</sup>:

$$\mu = (e/k) D/T \quad (6)$$

where  $T$  is the temperature of the gas. For intervals of time less than the delay time  $\alpha$  decreases rapidly which is evidenced by calculating the number of electrons remaining as a function of time and comparing the result with the measured efficiency of the chamber. It was noticed that the electrons are completely recombined as the chamber efficiency drops to zero within about 3 microseconds. The time dependence of  $\alpha$  is influenced mainly by the non-random initial distribution<sup>15</sup> of the electrons. Combining these results with Equation (3) the normal diffusion distance becomes

$$x = D_p P_c \int_{t_0}^t \frac{dt}{1 + \alpha n_0 t} \quad (7)$$

It is assumed that electron diffusion is directly related to the resolution of the chamber and which is seen in Figure 9 to be proportional to  $T^{3/2}$ , and is verified by completion of the integration in Equation 7 by numerical methods with time dependence of  $\alpha$  included.

Thus, calculations based on electron diffusion are in good agreement with the observed temperature dependence of the resolution. The temperature scale was adjusted to account for the liquification of the gas. This method was applied to the data reported by W. Willis<sup>2</sup> for high pressure spark chambers where the resolution was observed to depend

on pressure approximately as  $P^{-\frac{1}{2}}$  and is in good agreement with the diffusion theory. An obvious comparison between the pressure and temperature data is a more rapid decrease in resolution as the temperature is lowered. As the gas temperatures near the point of neon liquification even better resolutions are predicted.

The authors would like to express their appreciation to Dr. A. Roberts, Dr. J. Lach, Dr. S. Ecklund, J. Blomquist and J. Urish for their significant technical assistance and consultations.

#### REFERENCES

- <sup>1</sup>M. Atac, Nuclear Instr. and Methods 93 (1971) 521.
- <sup>2</sup>W. J. Willis, et al, Nucl. Instr. and Methods 91 (1971) 33.
- <sup>3</sup>Science Accessories Corporation, Southport, Connecticut.
- <sup>4</sup>J. Sayers, Roy. Soc. Proc. 169 (1939) 83.
- <sup>5</sup>L. L. Skolil, Phys. Rev. 70 (1946) 619.
- <sup>6</sup>B. Rossi, "High Energy Particles", (Text).
- <sup>7</sup>M. A. Biondi, Phys. Rev. 93 (1953) 1136.
- <sup>8</sup>M. A. Biondi, Phys. Rev. 75 (1949) 1700.
- <sup>9</sup>J. L. Lloyd. Phys. Soc. of London Proc. 75 (1960) 378.
- <sup>10</sup>L. Frommhold, M. A. Biondi, et al, Phys. Rev. 165 (1967) 44.
- <sup>11</sup>A. Salop and H. H. Nakano, Phys. Rev. 2 (1970) 127.
- <sup>12</sup>C. E. Normand, Phys. Rev. 35 (1930) 1217.
- <sup>13</sup>M. P. Lengevin, Ann. Chim. Phys. 28 (1903) 433.
- <sup>14</sup>H. J. Oskam and V. R. Mittelstadt, Phys. Rev. 132 (1963) 1435.
- <sup>15</sup>O. Luhr, Phys. Rev. 35 (1930) 1394.

- Fig. 1 A schematic cross-sectional view of the spark chamber liquid nitrogen assembly.
- Fig. 2 A front view of the wire plane and a more detailed cross-section of the spark chamber.
- Fig. 3 Spark voltage threshold versus temperature.
- Fig. 4 Scattergram of the deviations of particle trajectories from linear tracks as a function of the slope of the track.
- Fig. 5 Distributions of linear deviations from tracks for various spark chamber temperatures.
- Fig. 6 Efficiency of a spark chamber as a function of the delay time of the high voltage pulser.
- Fig. 7 Fractional energy loss of ionization electrons in neon (at temperature  $T$ ) as a function of time.
- Fig. 8 Diffusion coefficient of electrons in neon.
- Fig. 9 Resolution of the spark chamber at cryogenic temperatures.

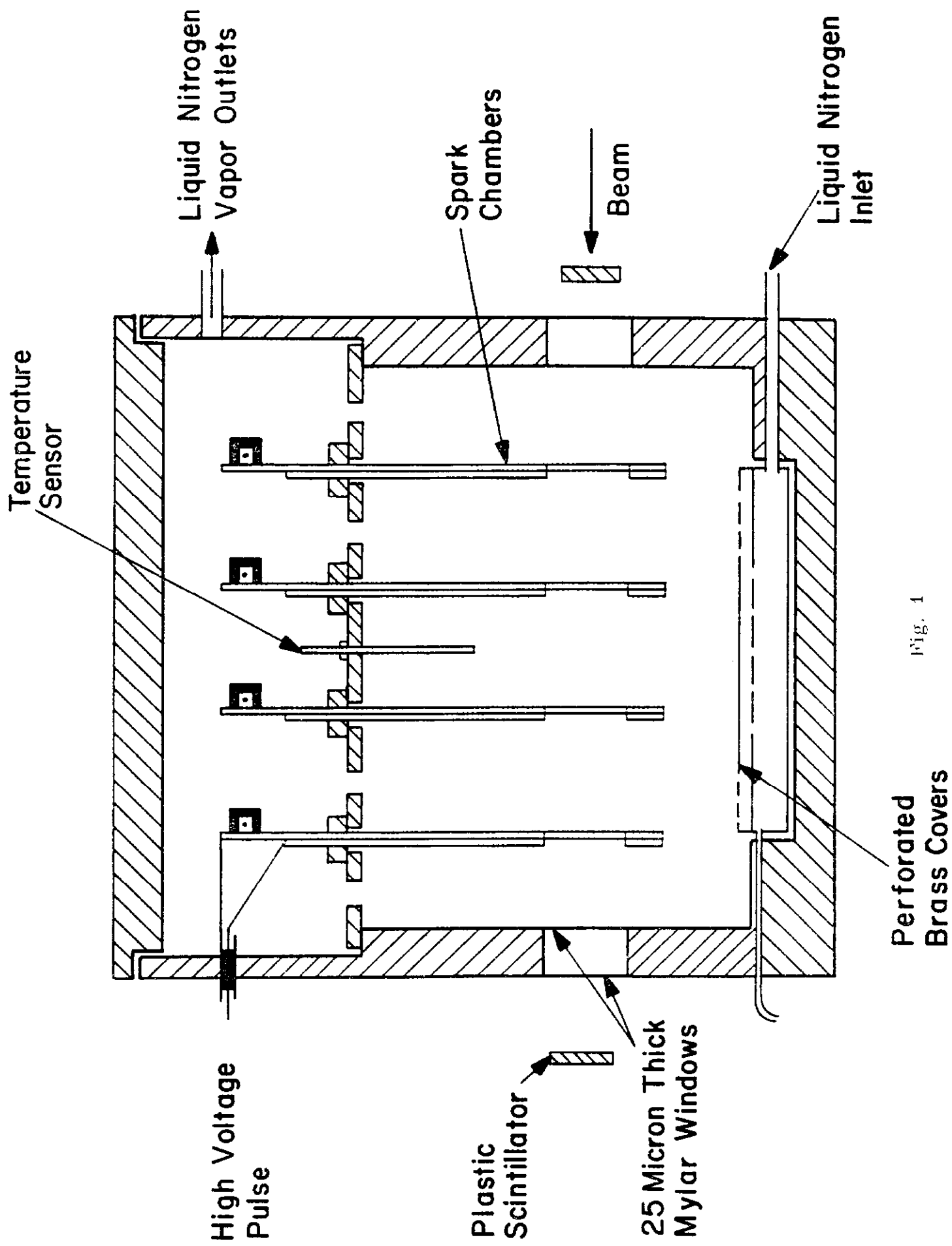


Fig. 1

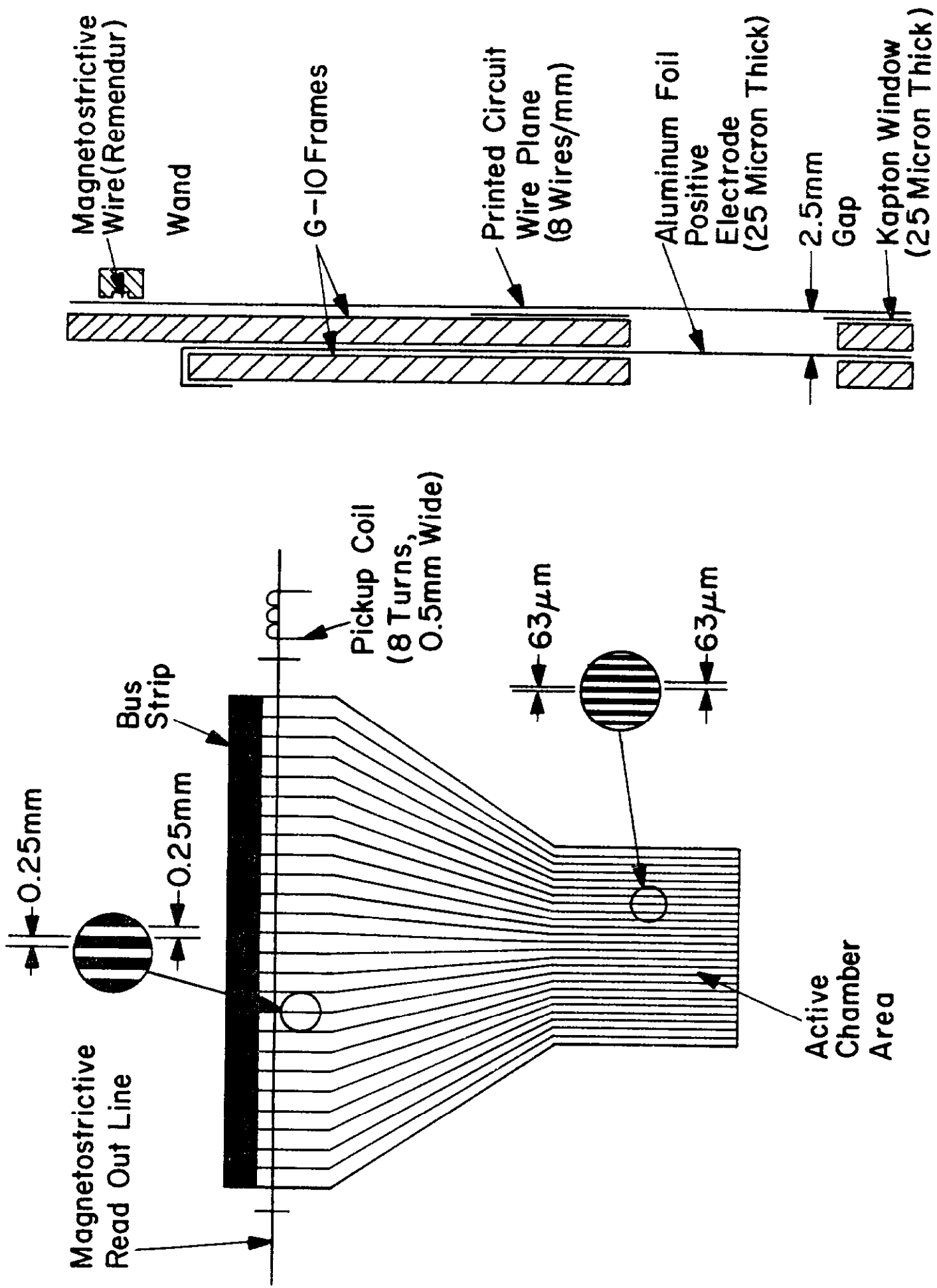
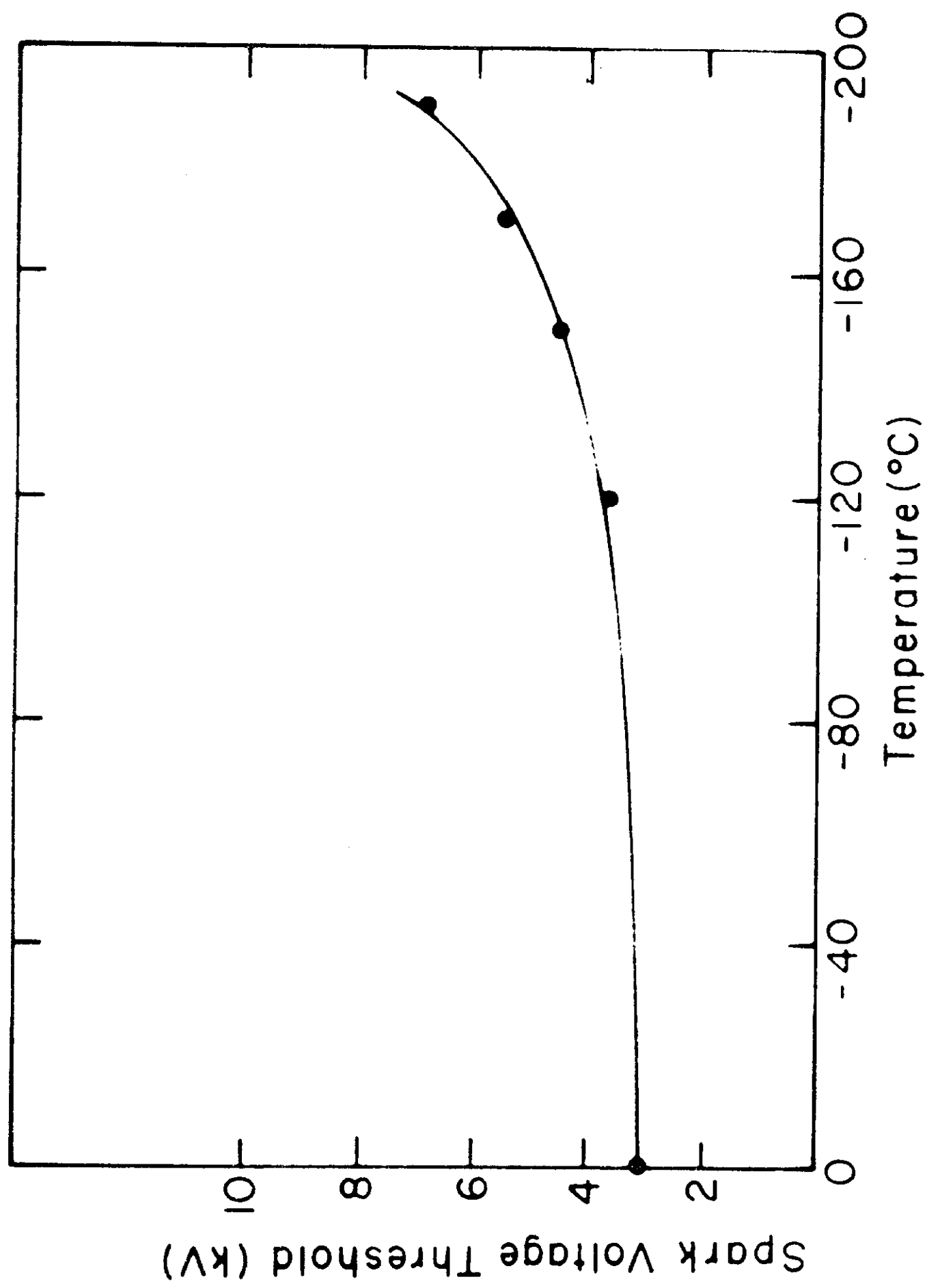


Fig 2



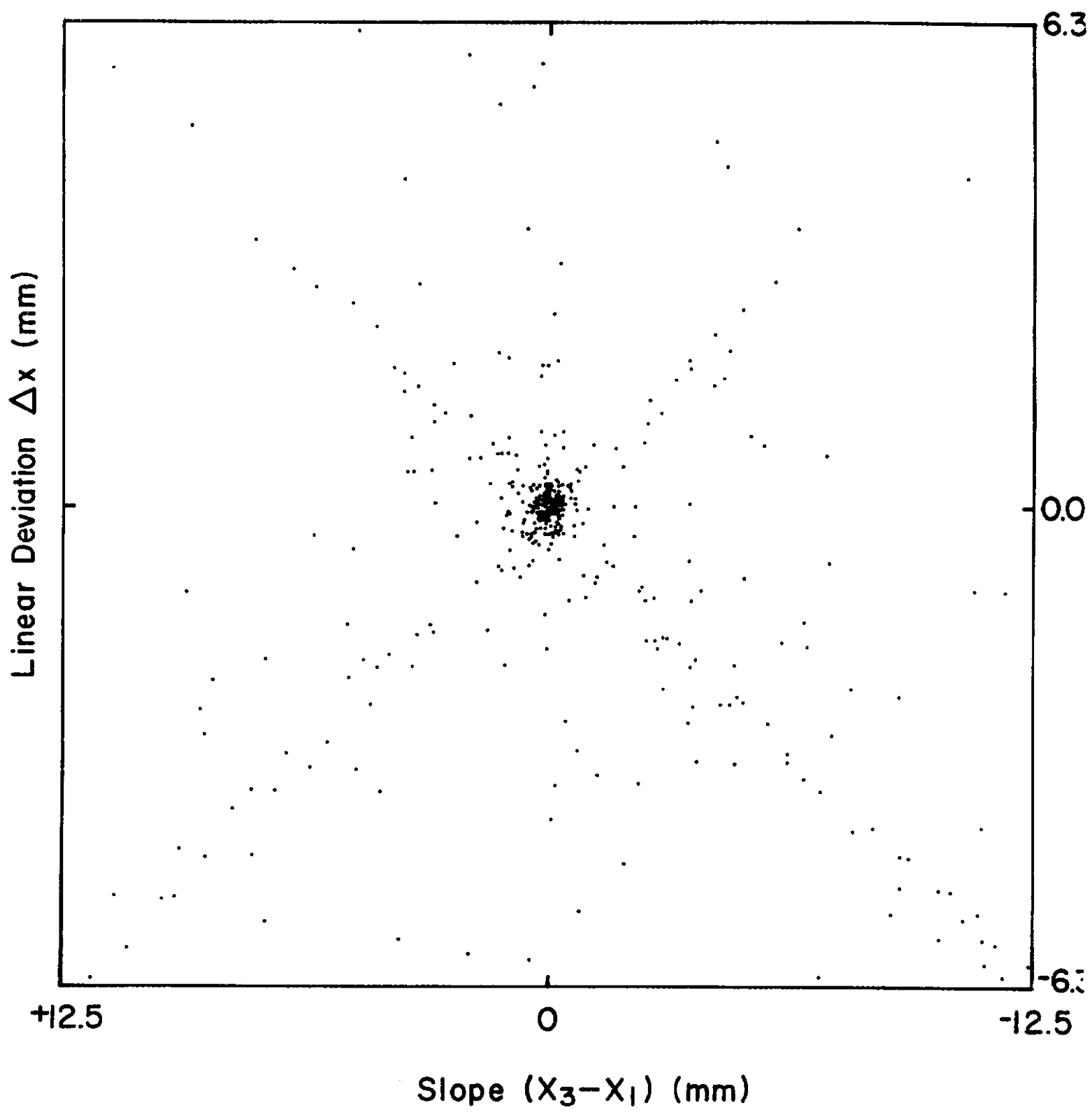
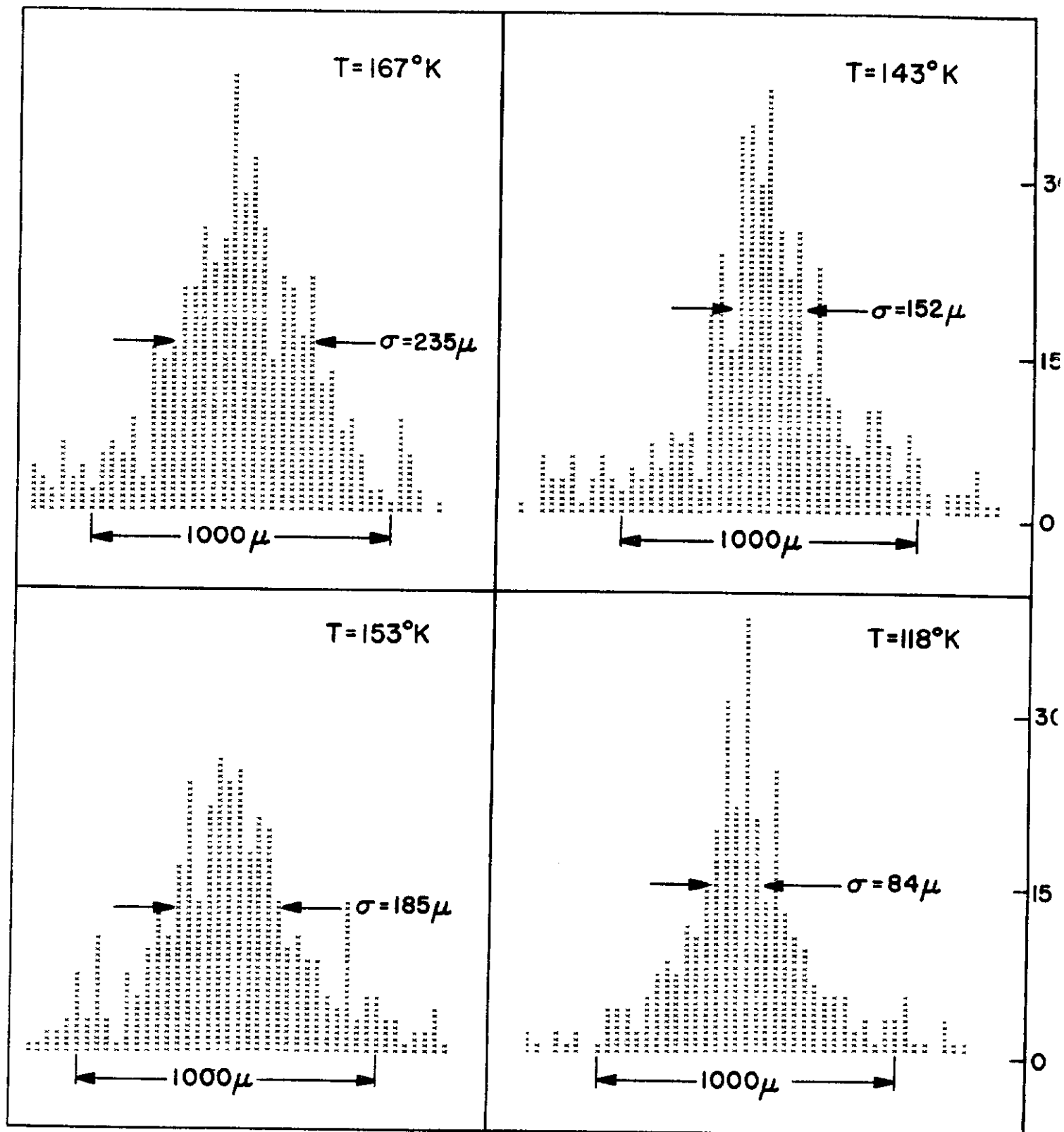


Fig. 4

Frequency of Events



Spatial Distribution of Deviations (Microns)



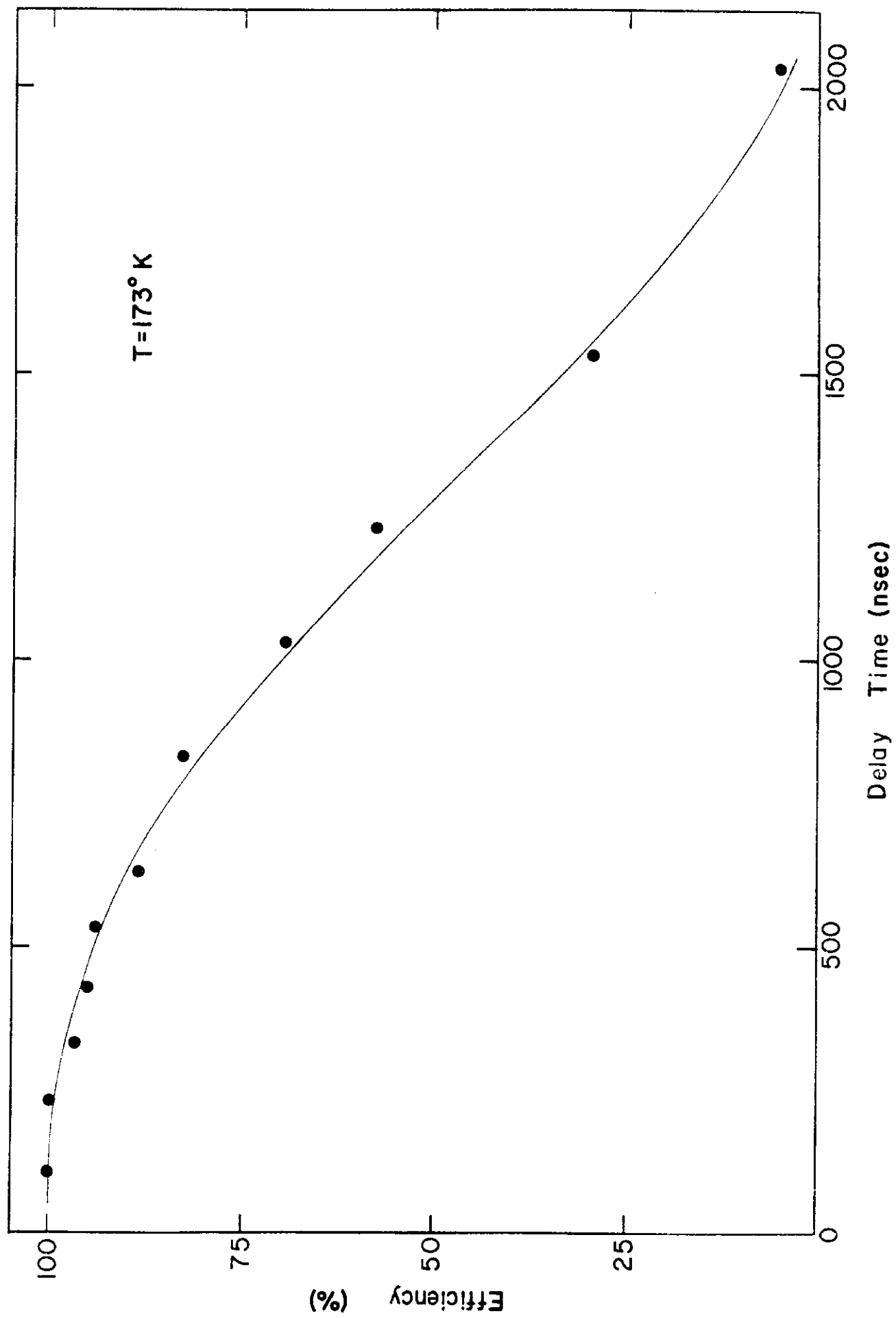
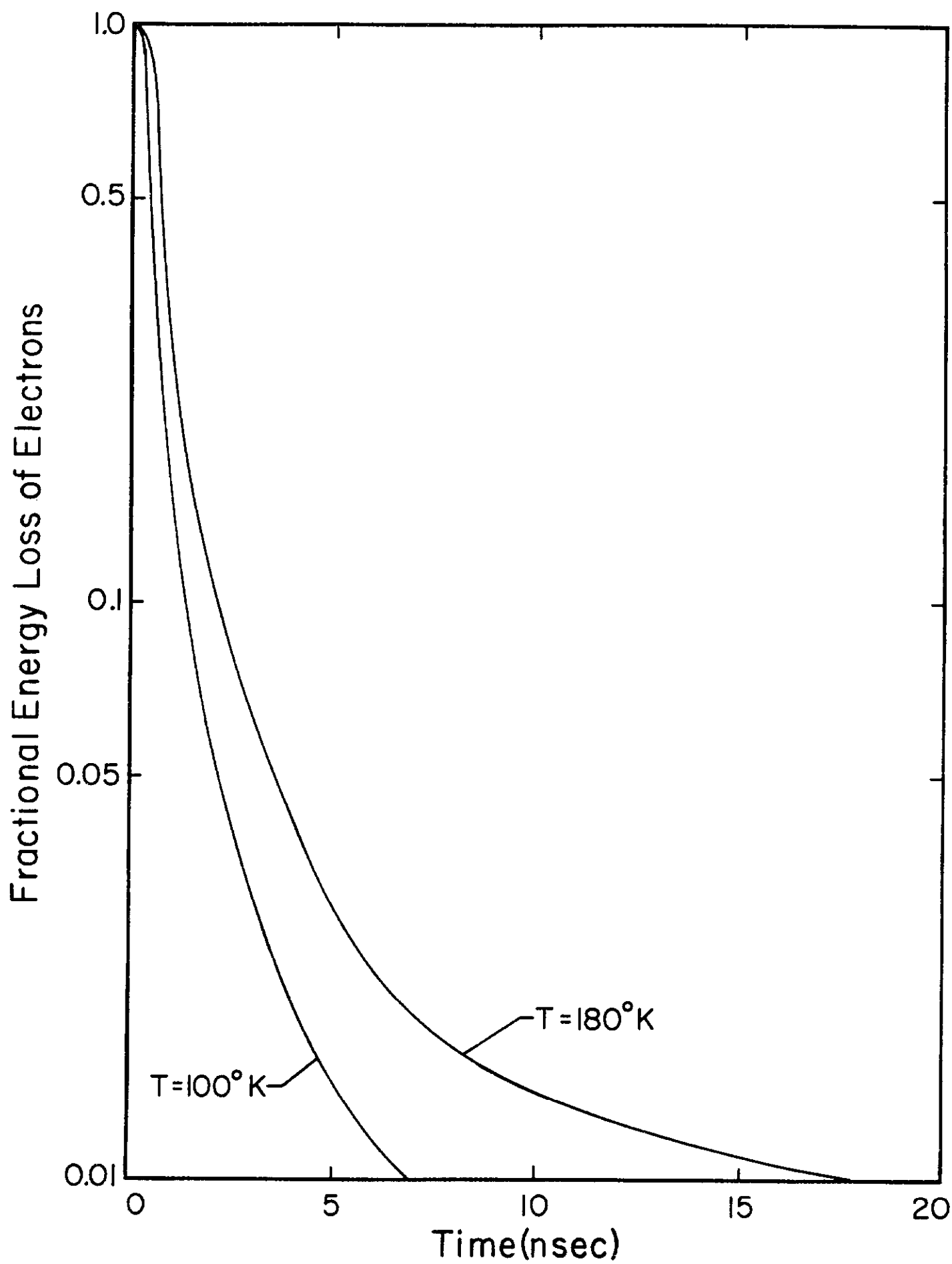
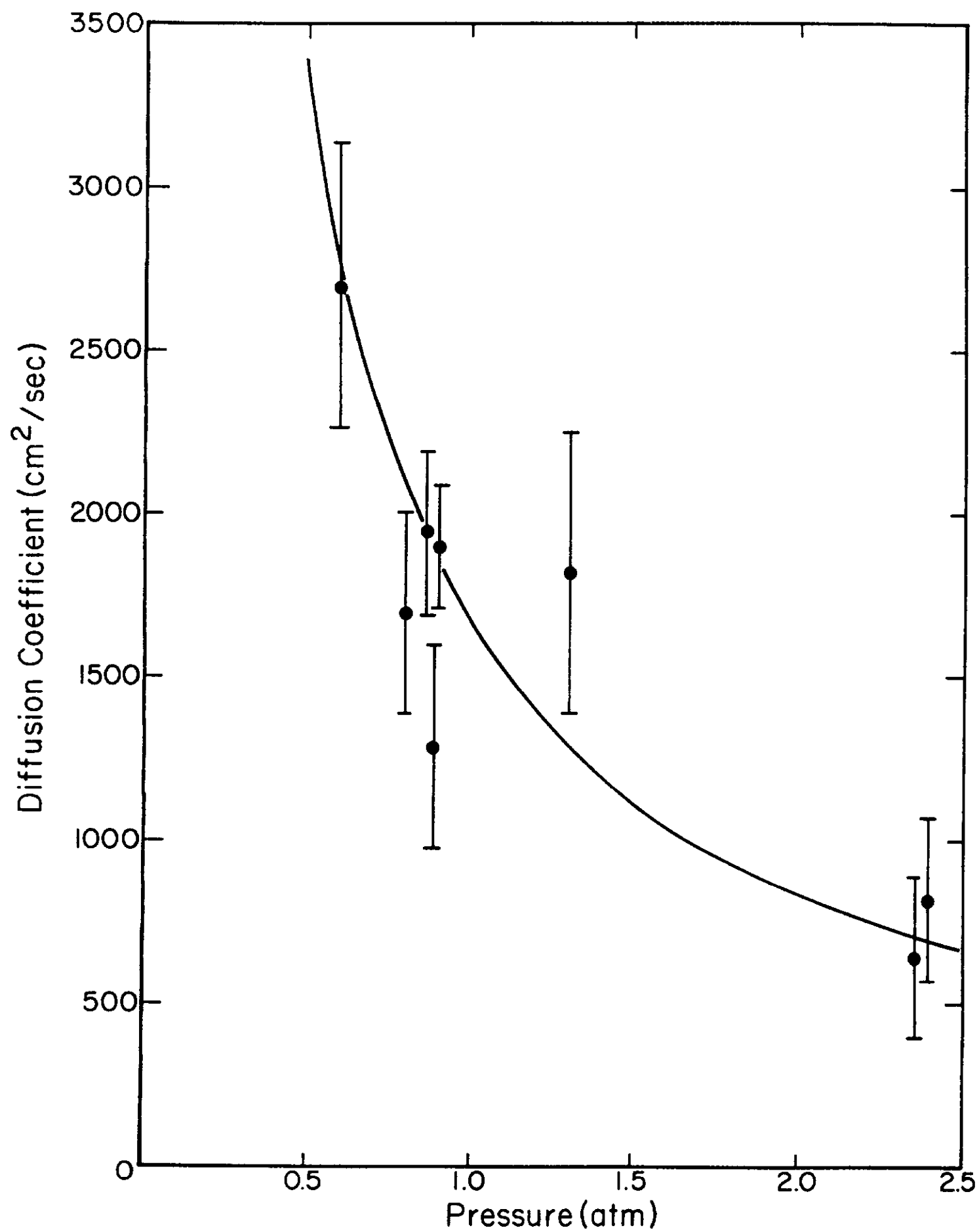


Fig. 6





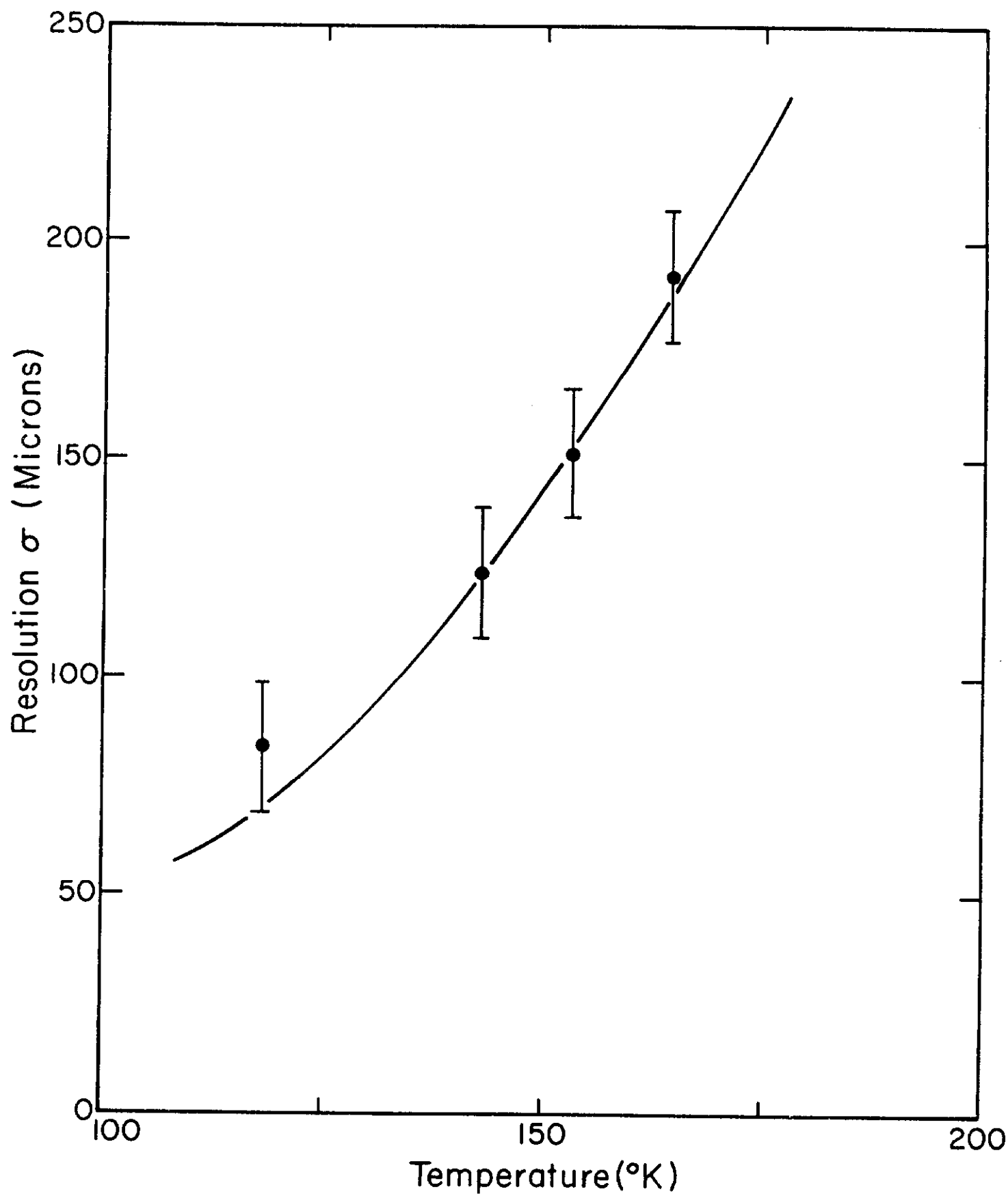


Fig. 9